


Article

A Study on Phase-Changing Materials for Controllable Stiffness in Robotic Joints

Bingyin Ma ^{1,2}, Mohammed Z. Shaqura ^{1,*} , Robert C. Richardson ¹ and Abbas A. Dehghani-Sanij ¹

¹ Institute of Design, Robotics and Optimisation, School of Mechanical Engineering, University of Leeds, Leeds LS2 9JT, UK; b.y.ma@hotmail.com (B.M.); r.c.richardson@leeds.ac.uk (R.C.R.); a.a.dehghani-sanij@leeds.ac.uk (A.A.D.-S.)

² London South Bank Innovation Centre, Cambridge CB21 6AL, UK

* Correspondence: m.z.m.shaqura@leeds.ac.uk

Abstract: This paper studies the viability of using a class of phase-changing materials for the design of controlled variable stiffness robotic joints which enable the design of robots that can operate in confined spaces. In such environments, robots need to be able to navigate in proximity or while in contact with their environment to reach one or more manipulated target. Joints with controllable stiffness can substantially enhance functionality of this class of robots where relatively higher joint stiffness is required to support the robot weight against gravity and low stiffness is desired when operating in complex or delicate environments. The research work presented in this paper focuses on examining thermorheological fluids (TRF) to design and manufacture thermally controlled variable stiffness joints. Two phase-changing materials are considered in the study: low-melting-point solder and hot-melt adhesive. Both materials are embedded in a custom designed joint fabricated using 3D printing and silicone casting. Joint stiffness was investigated with both materials and reported here. The results shows that the proposed variable stiffness joints with TRF achieve wide ranges of load-deflection ratio varying between 0.05 N/mm (when thermally activated) to about 10 N/mm (in bonding state). On average, the joint can withstand 20 times its total weight when in the bonding state. Design challenges and durability of TRF-based joints are discussed.

Keywords: variable stiffness; thermally activated joints; thermorheological fluids; phase-changing materials; robotic joint design



Citation: Ma, B.; Shaqura, M.Z.; Richardson, R.C.; Dehghani-Sanij, A.A. A Study on Phase-Changing Materials for Controllable Stiffness in Robotic Joints. *Robotics* **2022**, *11*, 66. <https://doi.org/10.3390/robotics11030066>

Academic Editor: Giuseppe Carbone

Received: 20 April 2022

Accepted: 14 June 2022

Published: 16 June 2022

Publisher's Note: MDPI stays neutral with regard to jurisdictional claims in published maps and institutional affiliations.



Copyright: © 2022 by the authors. Licensee MDPI, Basel, Switzerland. This article is an open access article distributed under the terms and conditions of the Creative Commons Attribution (CC BY) license (<https://creativecommons.org/licenses/by/4.0/>).

1. Introduction

The variable stiffness joint design and TR fluids characterisation discussed in this work can be applied to various applications of robotics. Snake-like robots will be used as a direct application and objective behind this development. Snake robots represent a unique class of bio-inspired mobile robotic platforms. Its uniqueness lies in its ability to operate within unusual and minimally structured environments which often require high levels of adaptability and accuracy. These robots consist of several serially connected joints that allow the robot body to follow complex trajectories mimicking the mobility of biological snakes. These robots are well suited for operating in complex and non-uniform environments where the body of the robot should bend around obstacles to reach a target point to perform an inspection or a manipulation task [1].

Snake robots can be classified based on their actuation mechanisms placement which can be distributed or centralized. Robots with distributed actuators have their driving components mounted across the whole length of the structure, each actuator drives one or more joints [2,3]. Distributed actuator configuration enables a robot to achieve a small radius of curvature, utilising a high number of degrees of freedom, which makes them ideal for grasping or latching applications. The challenge remains in the overall weight of the robot and distribution of mass. Actuators distributed across the snake body greatly increase the cascaded load and therefore reduces the robot's capability for self-support, i.e., the

number of body sections that can be lifted against gravity is limited. Furthermore, their joints have relatively large cross-section areas to accommodate the distributed drivers [4,5]. Centralised actuation uses one or more driving devices that are positioned at a reference robot base. Joints are normally controlled using tendons (wires) [6–8]. This configuration eliminates substantial load acting on the actuators and allows designs of longer self-supported structures and slender cross-sections. Due to their structure and sometimes the complexity of the wire mechanism, the range of deflection for each joint is lower compared to the distributed actuation configuration.

Robotic joints forming the snake robots can be categorized based on the build material. Hard rigid joints are less likely to be affected by external forces, hence, achieving high movement and manipulation accuracy. Soft joints are constructed from soft compliant materials (e.g., silicone, rubber, and springs), while the impact of soft joints on its surroundings is relatively low, the amount of loading force it can withstand is limited [9,10], while hard manipulators pose a high level of accuracy, they lack in general the ability to alter rigidity or stiffness when needed [11,12]. Stiffness control can be achieved using friction between joints to modulate the overall stiffness [13–15]. Three cables are passed along the body of a hollow multi-link robot to steer the tip using antagonistic forces. Applying tension on the wires causes friction at the interface between the joints resulting in increasing the stiffness of the overall structure. The control of such mechanisms is complex and often results in limited joint deflection and a smaller overall bend radius. Soft joints pose substantially larger compliance to adapt to geometric features of their surroundings [9]. This flexibility usually comes at the expense of constraining the manipulation force.

Variable stiffness techniques become game changers to address the challenges facing soft joint accuracy and maximum force. Stiffness modulation enables hard and soft robots to interact with their environments more effectively [16]. Softness enables dexterity and prevents damage to the environment, whereas rigidity increases the threshold of the applied force and accuracy. The growing interest in stiffness modulation has led to an increased interest in smart materials. Specifically, materials that can rapidly and reversely vary in stiffness. Examples include magnetorheological (MR) fluids [17], electrorheological (ER) fluids [18,19], thermorheological (TR) fluids [20–23], and granular materials [24–28]. MR and ER fluids have fast transition times and good range of stiffness change. However, they suffer from low repeatability, i.e., fluids are subjected to thickening after prolonged use. TR fluids are an interesting solution to realize stiffness modulation. There have been a series of attempts with wax, hot-melt adhesive [29,30], and low-melting-point alloy [31,32], to create controllable stiffness elements in soft robots. These studies focus on the activation and torque characterisation of these materials or focus on joint design considerations. We offer here a comprehensive study on (TRF) navigating through the characterisation setup, joint design, simulation, and fabrication while highlighting the potential and limitations of these materials for controlled stiffness robotic joints. Jamming is a popular technique to achieve variable stiffness. Granular jamming uses vacuum pressure to cause powder materials to transition between solid-like and fluid-like states. It requires a large volume of granular materials to achieve the desired stiffness and suffers scalability challenges to make it smaller or lighter. A controllable stiffness origami skeleton is presented in [33], a vacuum-powered cube is able to achieve various poses and withstand a few hundred grams of load. Precision manipulation could be a challenge for a fully soft structure. The vacuum interface can introduce controllability limitations. In [34], the authors discussed the design of a thermally activated variable stiffness mechanism for a soft finger. The study is particularly interesting as it introduces a hybrid structure with a soft and rigid part and the effect of temperature on the soft material. Another approach is shown in [35] where controlled stiffness is achieved via manipulating the interface area between the torque source and torque output interface using rotating fin hinges. This design addressed flexibility and precision but does not address softness and impact on the environment. The mechanism requires a relatively complex control system.

The work presented in this paper has two main objectives: 1. investigate the viability of using TR fluids as means of thermally controlled variable stiffness. 2. design a variable stiffness robotic joint that satisfies the design requirement. The maximum dimension of the joint is $5 \times 5 \times 9$ cm and the maximum joint bend angle is 50 degrees. The maximum load when activated is less than 0.5 N and the minimum yield point in the bonding state is 5.5 N. The maximum angular velocity is 0.6 rad/s. The rest of the paper is organized as follows: Section 2 presents the experimental testbed to characterize the response and repeatability of the two materials considered in this study, low-melting-point solder and hot-melt adhesive. The design and simulation of a controlled stiffness joint are discussed in Section 3 before presenting the fabrication techniques to develop two types of joints in Section 4. Experimental validation and results discussion is presented in Section 5.

2. TR Fluids Characterization

Thermorheological fluids (TR fluids) materials bonding two surfaces are heated to alter the strength of that bond. Two TR fluids are considered in this study, hot-melt adhesive (HMA) and low-melting-point solder (LMPS). Before integrating these materials in the custom-designed joints, we experimentally studied the temperature effect on these materials and bonding repeatability. The designed testbed shown in Figure 1 consists of a heating element, a temperature controller, a k-type thermocouple, a layer of TR fluid, copper tape and wooden clamps. A thin layer of material is placed between two layers of copper tape to heat the material to its melting point. When heat is removed, a bond is formed as the material cools down.

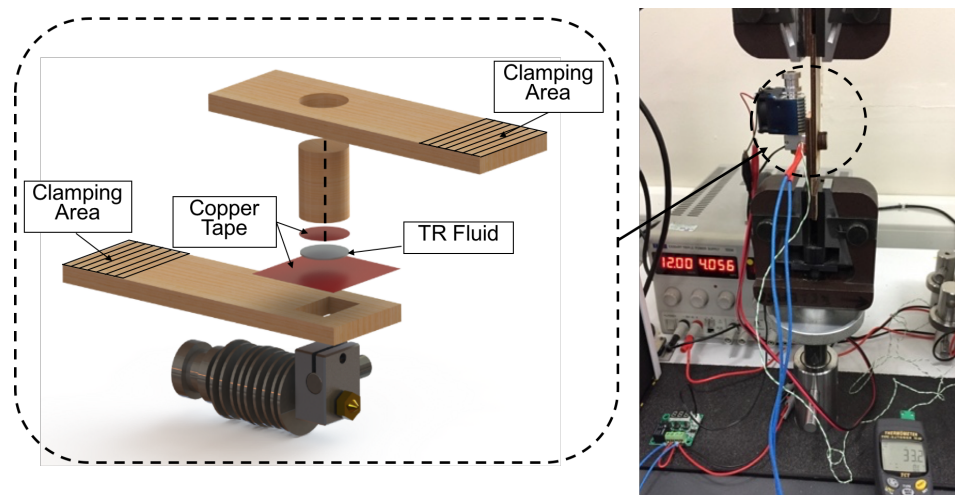


Figure 1. Testbed for TR Fluids Bonding Strength Response to Temperature Change.

2.1. Temperature Effect on Bonding Strength

The bonding strength is controlled by varying the applied heat. At melting points, TR fluid transforms to a semi-liquid state and the bond is easily broken. Field's metal and hot glue stick melting points are $62\text{ }^{\circ}\text{C}$ and $75\text{ }^{\circ}\text{C}$, respectively. The test assembly is clamped to an Instron test machine. The bond is broken at different temperatures between room temperature and melting point with about $5\text{--}10\text{ }^{\circ}\text{C}$ increments. The bonding area is measured afterwards and the temperature effect on the bond strength is obtained. Three independent trials are conducted for each material. Figure 2 shows the results of the effect of temperature on the bonding strength of LMPS and HMA. The average bonding strength of LMPS is approximately 1.65 MPa at room temperature. When the temperature reaches $50\text{ }^{\circ}\text{C}$, the bonding strength is reduced by about 8.32%. As the temperature rises above $62\text{ }^{\circ}\text{C}$, the bonding strength decreases by an average of 94.2%. The results from the HMA trials show that as the temperature increases, the bonding strength exponentially decreases from 1.1 MPa at room temperature to 0.007 MPa at $70\text{ }^{\circ}\text{C}$ near its melting point. The differences in bonding strength between the three trials is due to different temperature

increment, ambient temperature, and material application. Looking at the results from Figure 2, considerable effect on overall bonding behaviour is caused by a small variability in the amount of material applied or the distribution of that material over the host surface. Both material poses nonlinear bonding strength change with increasing temperature which affects the selection of the range of operation and application. LMPS response forms two regions with very small negative slope linear behavior switched at approximately 64 °C. This makes LMPS more suitable for applications where intermittent increased stiffness is needed. The temperature control resolution required for finely tuned stiffness will be challenging to achieve. HMA effective operating range can be set below 50 degrees for well spaced bonding variations. The heating and temperature feedback system specifications helps in precisely defining the range based on the characteristics.

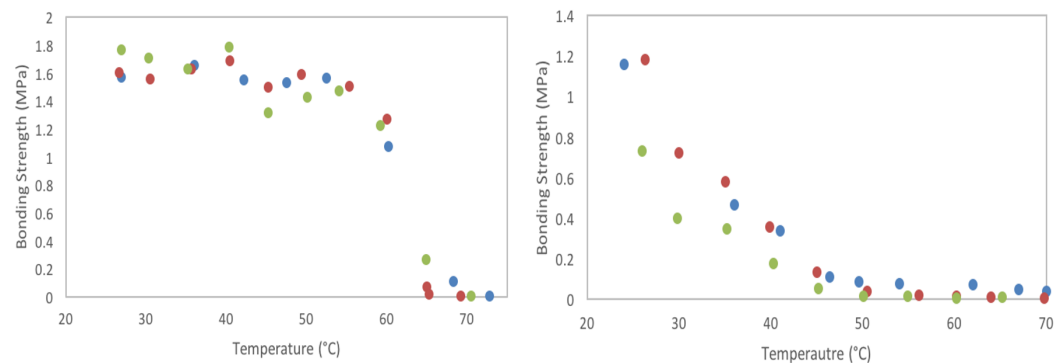


Figure 2. Temperature response of bonding strength of LMPS (left) and HMA (right). The bonding strength is the ratio of the bond breaking force to the bonding area. Each color represents the results from one of the three trials

2.2. Repeatability

The transition between solid and fluid states repeatedly can affect the strength of the bond created. To study the repeatability of LMPS and HMA bonding force, repeated heating–cooling experiments are conducted for each material. The same testbed used to study temperature response is used—Figure 1.

The material is heated to a near melting point temperature. Then, the cylindrical wooden part, where the top copper tape is glued, is rotated around its central axis to mimic the motion of a robotic joint. The heat is removed afterwards and the material cools down to room temperature forming a bond again. The new bond is broken by the Instron test machine. The bonding area is measured after the separation and the bonding strength is obtained after each trial. Three trials are carried out, each trial consists of 80 repetitions and each repetition contains one cycle of heating-rotating-cooling. The same amount of TR fluid is used to form a bond in each trial. The bonding strength is evaluated after 20, 40, 60 and 80 repetitions. The results of the bonding strength of LMPS and HMA over repetition are shown in Figure 3. Bonding strength steadily decreases as we repeat the experiment. The bonding strength of LMPS is reduced by 17.8% after 20 repetitions and by 19.2% after 80 repetitions. The bonding strength of HMA decreases by 16% after 20 repetitions and by 24% after 80 repetitions. The bond breaking point reduction is caused by the loss of mass of bonding materials due to the rotational motion of the cylinder.

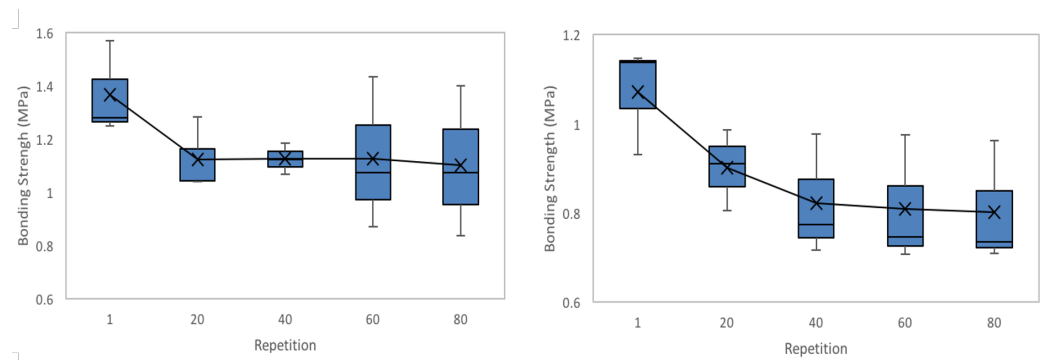


Figure 3. Results from repeatability experiments showing the decrease of bonding strength of LMPs (left) and HMA (right).

2.3. Adherend-Dependent Bonding Strength

The TR fluid formed bond strength is affected by the adherend material. To understand this effect, direct shear tests between different types of adherend surfaces were conducted. The construction material should be light and easy to use for joint fabrication. Three materials are compared using HMA and shear test: aluminium, copper, and plastic (VeroWhitePlus). Two plates (80 mm × 30 mm) made of the selected adherends were pre-treated to form effective bonds. The HMA is melted and applied between the two plates. The bond is shortly formed at room temperature. The plates are clamped to an Instron test machine, Figure 4, where the two plates are pulled apart and the shear force needed to break the bond is recorded accordingly.

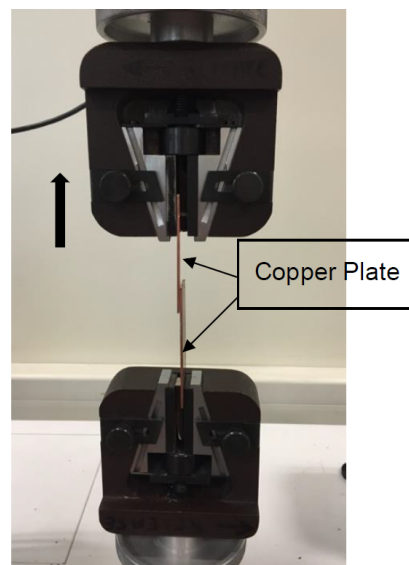


Figure 4. Experimental setup for adherend-dependent of bonding strength test. Two copper plates were glued together by HMA.

Table 1, shows the results of shear strength and variations of five trials between HMA and each adherend material. The bonding area was measured after the separation of plates. Shear strength was calculated as the ratio of shear force to bonding area. A material with higher shear strength is normally the choice for this application. We note that the shear strength in the case of aluminium and copper is very close. Copper is selected as an adherend interface due to its higher thermal conductivity (401 W/mK) compared to aluminium (205 W/mK), and hence helps in reducing the energy required for heating.

Table 1. Shear strength between HMA and candidate materials.

Material	Shear Strength (MPa)
Aluminium	1.0562 ± 0.1770
Copper	1.0496 ± 0.2443
Plastic	0.1846 ± 0.0373

3. Controllable Variable Stiffness Joint Design and Simulation

A concept design of a snake-like manipulator consisting of multiple homogeneous variable stiffness joints is shown in Figure 5 with the proposed designs of two types of joints, revolute and spherical joints. Wires are passed through the robot structure to steer the tip. Variable stiffness is achieved utilizing TR-fluids-based bonding mechanisms.

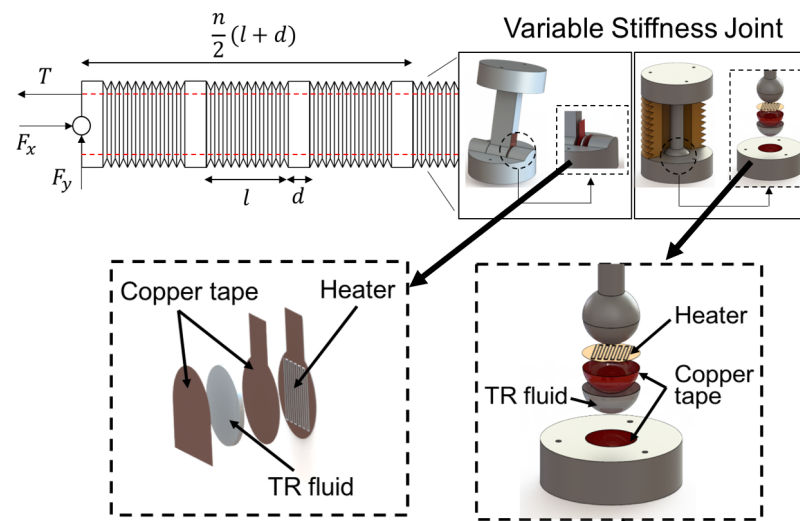


Figure 5. A concept design of a snake-like robot that consists of a number of revolute and spherical variable stiffness joints.

3.1. Design of Controllable Stiffness Joints

The controllable stiffness revolute and spherical joints are designed to achieve a bending range of $\pm 56^\circ$ satisfying the design requirement of a maximum bending angle of 50° . Figure 5 shows the CAD models of two types of joints employing TR-fluid-based bonding. The revolute joint consists of a silicone bellows-like structure, a thermally activated bonding mechanism, a joint shaft, and a base. The silicone bellows-like structure is designed to isolate the heat and prevent potential damage to the surrounding environment. The layer of TR fluid material (LMPS or HMA) is sandwiched between two copper tapes that are in direct contact with a resistive heating element. The stiffness modulation is achieved by activating the bonding mechanism: the joint can rotate freely when the TR fluid is heated and can be rigid at an arbitrary angular position by cooling the bonding material. Similarly, the spherical joint is composed of a thermally activated bonding mechanism, a silicone bellows-like structure, a spherical shaft, and a base. The TR fluid material (LMPS or HMA) is sandwiched between two copper tapes that are heated by a resistive element. The spherical joint can be steered by three wires passing through the base and the shaft.

A highly flexible silicone material (Ecoflex 0030) is selected to construct the bellows-like structure [36]. Silicone helps in isolating the heat generated during the thermal activation of bonding materials. The stress–strain relationship of silicone can be described as non-linear, isotropic, incompressible and generally independent of strain rate [37–39]. Material specifications are needed for accurate material modelling for nonlinear simulation in SolidWorks. Hyperelastic material models can be used to describe the stress–strain behaviour of silicone

material [40,41]. Ecoflex 0030 characterisation using hyperelastic models was discussed in [42,43] with a number of possible models to select from depending on the specifications of the used material. Assuming each joint can achieve an angular velocity of 0.6 rad/s, the time required to rotate to the desired bending angle of 56° can be estimated as:

$$t = \frac{\theta}{\omega} = \frac{56 \times 2\pi}{360 \times 0.6} \approx 1.6\text{s} \quad (1)$$

An Initial estimation is done to identify the range of strain for the silicone material. A drawing of a joint before and after bending is presented in Figure 6. The initial height of the bellows-like structure is 22.56 mm. When a joint is bent to 56° , the distances between the top and bottom caps are changed to 29.73 mm and 16.85 mm, respectively. The strain of the bellows-like structure can be calculated as:

$$\Delta\epsilon_1 = \frac{L_1 - L_0}{L_0} = \frac{29.73 - 22.56}{22.56} = 0.3178 \quad (2)$$

$$\Delta\epsilon_2 = \frac{L_0 - L_2}{L_0} = \frac{22.56 - 16.85}{22.56} = 0.2531 \quad (3)$$

The maximum strain of the robotic joint is estimated as 31.78%. The estimated strain rate can be computed as ($d\epsilon = \frac{0.3178}{1.6} \approx 0.1968\text{s}^{-1}$).

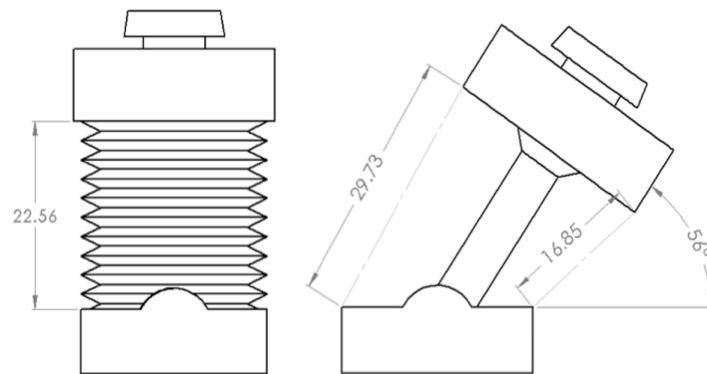


Figure 6. A revolute joint at home position (left) and at 56° angle (right).

To account for any potential impurities, we have experimentally identified the best model that fits the input–output data of the material we prepared. A uniaxial tensile test is a common approach to determining mechanical properties of materials [44]. The tests are done for five silicone strips, using a Mecmesin tensile testing machine with a 10 N load cell, at a speed of 500 mm/min. Figure 7 shows the average data of five trials. The strain rate of silicone Ecoflex 0030 under 500 mm/min test speed is 0.1911 s^{-1} . Note that the value obtained analytically closely resembles the experiment output. Data from the test is fitted using a hyperelastic model that is used in the finite element analysis (FEA). Several hyperelastic material models, such as Neo-Hookean, 3-term Mooney-Rivlin model, 5-term Mooney-Rivlin model, 3-term Yeoh model, 2-term Ogden model, and Arruda-Boyce model are considered to fit the experimental data. The sum of square errors is used to determine the most appropriate model that describes the material [37]. A 5-term Mooney-Rivlin model with parameters ($C_{10} = 0.0041$, $C_{01} = 0.0079$, $C_{11} = 0.0194$, $C_{20} = -0.0074$, and $C_{30} = -0.0108$) is selected to model the flexible bellows-like structure.

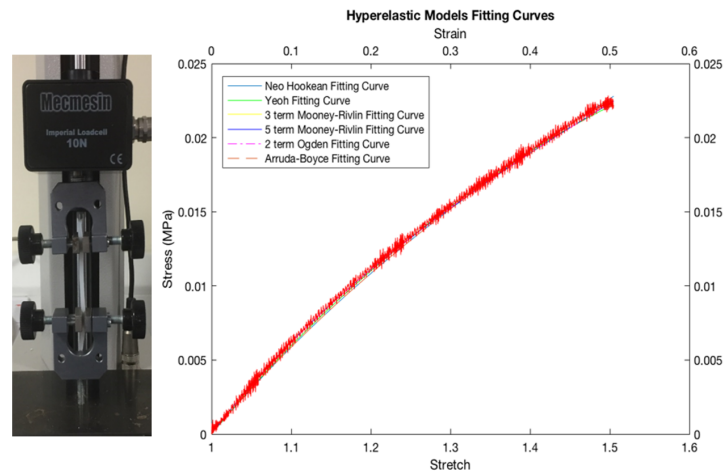


Figure 7. Tensile test results of Ecoflex 0030. Test setup (left). Stress-strain data was fitted using hyperelastic models (right).

Joints are simulated in SolidWorks to validate the strain estimates. The joint is cantilevered, and an external load is applied to the end-effector of the joint. The contact condition between the bellows-like structure and revolute joint/spherical joint is set to be bonded. Solidworks simulation results of the revolute and spherical joints bending are shown in Figure 8. When the joints are subjected to 56° bending angle, the maximum strains are 0.489 and 0.443 for the revolute joint and the spherical joint, respectively.

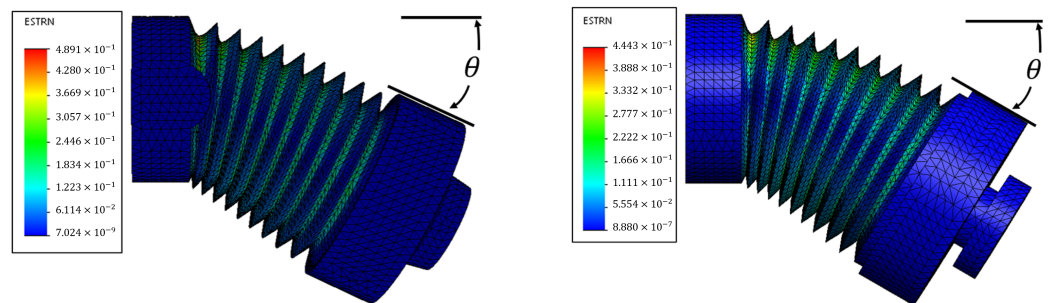


Figure 8. Maximum strain of a revolute joint (left) and a spherical joint (right) at 56° bending angle.

3.2. Bonding Torque Analysis

To determine the torque required to lock the manipulator at an arbitrary position, an extreme configuration is considered where a manipulator is placed in a cantilevered position. The torque affecting each joint is directly proportional to the total weight and the distance between the joint and the fixed end of the manipulator, refer to Figure 9. To maintain the manipulator at a cantilevered state, the bonding torque should be greater than the torque imposed by the weight of the manipulator.

$$T_{\text{bond}} > T = W.L \tag{4}$$

The bonding force is directly proportional to the material bonding strength and bonding area. Bonding strength calculation for LMPS and HMA are discussed in Section 2. The bonding strength on the differential elements (dA) generates a moment around the centre of bonding area. The differentials of bonding force and moment are given by:

$$dF_{\text{bond}} = \tau \cdot dA \tag{5}$$

$$dM = r(\tau \cdot dA) \tag{6}$$

The integration of the moment over the bonding area is equivalent to the bonding torque (T_{bond}) and the torque can be obtained by integrating in a polar coordinate system:

$$\int_A dM = \int_A r(\tau \cdot dA) = T_{\text{bond}} \tag{7}$$

$$T_{\text{bond}} = \tau \int_0^{2\pi} \int_0^R r^2 dr d\theta = \frac{2\pi}{3} \tau R^3 \tag{8}$$

where R denotes the radius of the bonding area. Given the length and weight of the manipulator, the bonding torque that is required to hold the manipulator at an arbitrary position can be computed.

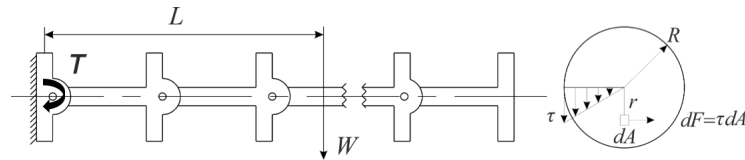


Figure 9. A Snake-like manipulator consists of a number of revolute joints in a cantilevered configuration.

The bonding torque of spherical joints is calculated on the spherical surface. Figure 10 illustrates a simplified torsional model. The bonding area element is given by:

$$dA = 2\pi r dS \tag{9}$$

where r ($r = R \sin \theta$) is the radius of the cross-sectional area, R is the radius of the sphere, and dS represents the arc element ($dS = R d\theta$). The bonding torque can be computed knowing the material strength τ and the angle θ :

$$T_{\text{bond}} = 2\pi R^3 \tau \int_0^\theta \sin^2 \theta d\theta \tag{10}$$

The models in Equations (7)–(10) provide insights on the design of the robotic joints to meet bonding torque specifications. In our design, the radius of the circle ($R_{\text{revolute}} = 4.75$ mm) and the radius of the sphere ($R_{\text{spherical}} = 4.25$ mm). The dimensions were purposely selected slightly higher than the required values to account for possible small misalignment between the two surfaces separated by the TR fluids. Table 2 presents the results of the maximum bonding torque achieved by LMPS and HMA bonds.

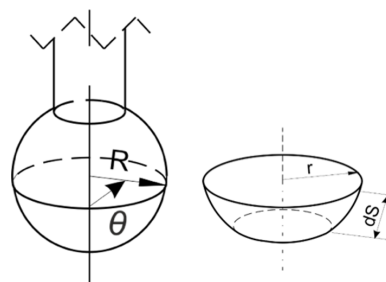


Figure 10. Torsional model (spherical joint). Bonding area is shown on the right.

Table 2. Bonding Torque Results of LMPS and HMA.

Joint Type	LMPS Bonding Torque	HMA Bonding Torque
Revolute Joint	336.75 Nmm	240.46 Nmm
Spherical Joint	495.79 Nmm	356.47 Nmm

3.3. Joint Stiffness Simulation in Rigid and Soft States

Finite element analysis in SolidWorks is used to simulate the designed joints and estimate stiffness in the rigid and solid states. An external force is applied to the joint and the resulting displacement is measured. Stiffness constant K is the ratio of the applied force F to the deflection δ ($K = \frac{F}{\delta}$). In this simulation study, we assume that the joints can achieve a complete shape lock when it is in a bonding state. In other words, the bonding materials do not contribute to the deflection of the module. It is also assumed that when the bonding material is activated, the bonding strength is zero. The contact condition between the shaft and base is set to ‘no penetration’ and the coefficient of friction is 0.3. The contact condition between the bellows-like structure and joint is set to ‘bonded’.

The revolute and spherical joints are cantilevered in the simulation. An external load is applied at the free end of the joint to simulate the effect in bonding (rigid) and activated (soft) states. The simulation results in Figure 11 show the joint strain caused by the applied force in both states. The displacement is assumed to follow a linear behaviour (the assumption will be validated through experiments in Section 5). The external loads used in the simulations are 600 g (5.88 N) and 20 g (0.196 N) in the rigid and soft states, respectively. The measured displacement, the maximum strain and stiffness constant are presented in Table 3.

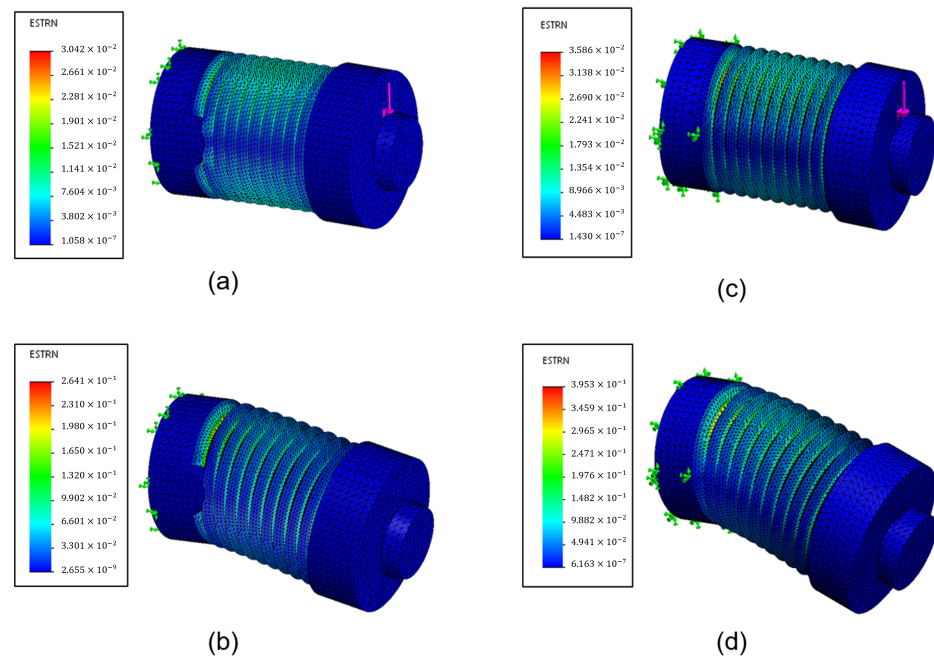


Figure 11. Simulation of a joint response to external load: (a) revolute joint in bonding state. the external load is 5.88 N resulting in a maximum equivalent strain of 0.03042. (b) revolute joint in a soft state. The external load is 0.196 N resulting in a maximum equivalent strain of 0.2641. (c) spherical joint in bonding state. the external load is 5.88 N resulting in a maximum equivalent strain of 0.03586. (d) spherical joint in a soft state. The external load is 0.196 N resulting in a maximum equivalent strain of 0.3953.

Table 3. Simulation Results of the Revolute and Spherical Joints in Bonding and Soft States. ‘R’ refer to revolute joint and ‘S’ refer to spherical joint.

State	Load	Displacement	Max Strain	Stiffness Constant
Bonding (R)	5.88 N	1.101 mm	0.03042	5.3406 N/mm
Soft (R)	0.196 N	7.291 mm	0.2641	0.0269 N/mm
Bonding (S)	5.88 N	1.174 mm	0.03586	5.0085 N/mm
Soft (S)	0.196 N	11.488 mm	0.3953	0.0171 N/mm

3.4. Joint Heating and Cooling Processes

Heating energy is consumed to increase the joint temperature and change the phase of TR fluids. We assume the heat loss during the heating process is negligibly small. In some cases where the heat loss might be significant based on operating conditions and heating techniques, the heating model can be updated to incorporate that, hence the model provided here results in a lower bound on melting time. The energy Q_{TR} required to melt the TR fluids can be expressed by the equation,

$$Q_{TR} = mc(T_{melting} - T_0) + mL_f \quad (11)$$

where m is the mass of TR fluid, c is the specific heat capacity of the material, $T_{melting}$ is the melting temperature of the fluid, T_0 is the initial temperature of the material, and L_f is the material’s latent heat fusion. Melting time t can be estimated using the input energy Q_{TR} and power of the heater P_{heater} ,

$$t = \frac{Q_{TR}}{P_{heater}} \quad (12)$$

The heating time model provides an insight into consumed energy. Materials with low-melting-point temperature and low specific heat capacity and low latent heat fusion are desirable. The amount of material (mass) decrease leads to faster heating but can result in lower bonding strength.

In the cooling process, heat is transferred in the opposite direction. Figure 12 shows a schematic of the heat path through the joint during cooling. The energy source is the TR fluid. The solidification energy of the TR fluid must be lost for the joint to enter the rigid state. The solidification energy can be calculated as,

$$Q_{solid} = mc(T - T_{solidus}) + mL_f \quad (13)$$

T is the temperature of the TR fluids at the beginning of the cooling process, $T_{solidus}$ is the solidus temperature of the materials, and L_f represents the heat fusion of the TR fluid. The heat transfer rate during cooling can be estimated as,

$$q = \frac{T - T_{solidus}}{R_{sink}} \quad (14)$$

where T represents the temperature of the heat sink components at the beginning of the cooling step, R_{sink} is the thermal resistance of the heat sink component.

$$R_{sink} = \frac{L_{heat}}{A_k k} \quad (15)$$

where L_{heat} is the length of the heat travel path, A_k is the conduction area, and k is the thermal conductivity of the material. The cooling time is,

$$t = \frac{Q_{solid}}{q} \quad (16)$$

The model provides insight on how to reduce cooling time. For example, the design of the heat sink is important to the cooling step. Shorter heat travel path and reduced mass results in faster cooling.

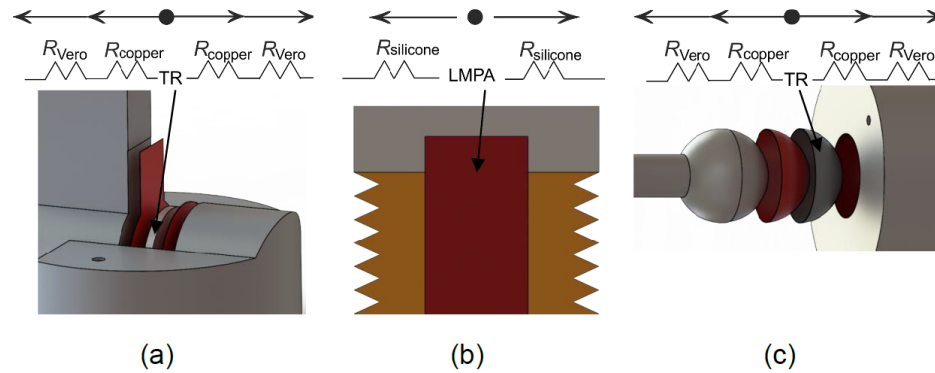


Figure 12. Heat path of the single module during cooling process. (a) heat path of LMPS- and HMA-based single module (revolute joint). (b) heat path of LMPA-based single module. (c) heat path of LMPS- and HMA-based single module (spherical joint).

4. Robotic Joint Fabrication

The proposed robotic joints consist of rigid plastic components (shaft and base), a silicone bellows-like structure and a thermally activated bonding mechanism. The plastic components are 3D printed using VeroWhite Plus material and Stratasys Objet 1000 printer. The fabrication of the bellows-like structure and the thermally activated bonding mechanism are discussed in this section.

4.1. TR Fluids Application

Due to the high surface tension and low reactivity with other metals, it is impossible to apply LMPS (Field’s Metal) to the surface of the copper tape without pre-treatment [22]. Flux is commonly used for preparing surfaces in electronics applications. Flux is used to pre-treat the copper surface before applying Field’s Metal, see Figure 13. First, flux is applied to the surface of the copper tape using a cotton swab. Then, the pre-treated copper tape is dipped into Field’s Alloy at approximately 200 °C. As a result, the surface can be fully covered by Field’s Metal. Flux residue was cleaned with warm water.



Figure 13. The method for applying Field’s Metal to the surface of copper tape. (Left) Applying flux on the surface of copper tape. (Middle) Dipping the copper tape into melted Field’s Metal. (Right) The pre-treated surface of the copper tape is covered by Field’s Metal.

To apply the HMA material, the copper tape is preheated by a hotplate to raise the surface temperature above the melting point of the used glue stick. Then, a piece of glue is placed over the heated surface of the copper tape which causes the meltdown of the material. The bond is formed when the source of heat is removed and the material cools down.

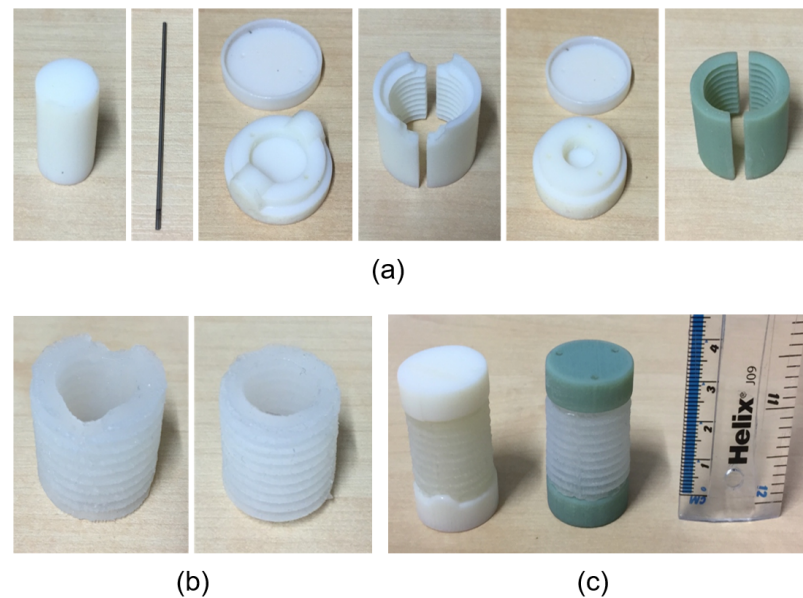


Figure 14. (a) The mould for the fabrication of the bellows-like structure. (From left to right) Cylinder, stainless pin, top and bottom cap for fabricating bellows-like structure for revolute joint, bellows-like cylindrical components (bellows for revolute joint), to and bottom cap for fabricating bellows-like structure for spherical joint, and two bellows-like cylindrical components (bellows for spherical joint). (b) Bellows-like structure for revolute joint (left) and spherical joint (right). (c) Controllable stiffness revolute joint (left) and spherical joint (right).

4.2. Joint Fabrication

A mould is created to fabricate the bellows-like structure for the revolute and spherical joints, see Figure 14a. The mould consists of a top cap, a cylinder, two stainless steel pins, two bellows-like cylindrical structures and a bottom cap. The plastic cylinder is used to create a chamber to accommodate the material. The pins are used to create cable channels. Mixed components of the EcoFlux 0030 silicone material are well stirred and then put in a degassing chamber to remove air bubbles trapped in the liquid. The flexible bellows-like structure is fabricated by pouring the silicone material into the mould. Two stainless steel pins are then inserted into the bottom cap. The top cap seals the mould and keeps the pins in place. The silicone material is then cured for around four hours. The fabricated bellows-like structures for revolute joint and spherical joints are shown in Figure 14b.

The shaft and base of the joint are 3D printed using a resin material. Resistive heating wires are used to activate the bonding materials. The wires wind and are closely attached to copper tapes and both are glued to the joint shaft. The joint shaft is then mounted on the base. The fabricated silicone bellows-like structure is glued to the plastic components using Sli-Poxy Silicone Adhesive. The fabricated joints are shown in Figure 14c.

5. Experimental Validation

The experimental setup for the designed TR fluids based variable stiffness joint is shown in Figure 15. The joint is cantilevered, and a varying load is attached to its free end. The joint deflection is measured in the rigid and soft states for a range of external loads. The tests aim to validate the analytical model results of bonding torques and

stiffness constants estimation from the simulation results and provide insight into joint response time.

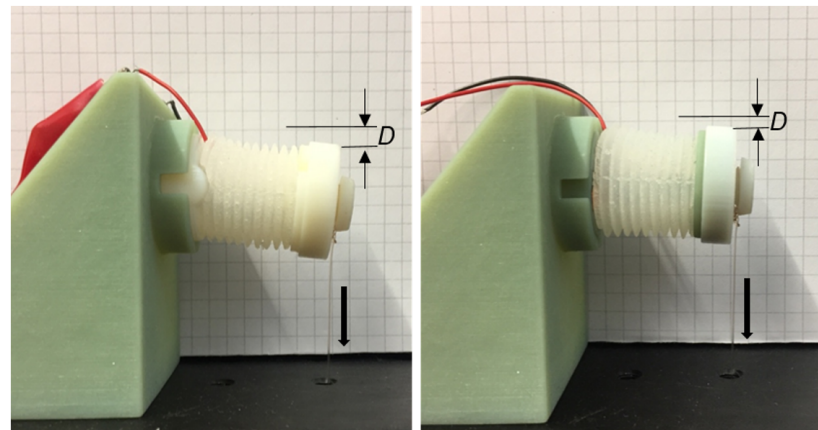


Figure 15. Test setup for TR-fluids based revolute joint (left) and spherical joint (right).

Four joint configurations are fabricated and tested: (1) LMPS-based revolute joint (LMPS(R)), (2) HMA-based revolute joint (HMA(R)), (3) LMPS-based spherical joint (LMPS(S)), (4) HMA-based spherical joint (HMA(S)). The joints are tested first in a bonding state at room temperature. An end-effector hook is designed and integrated with the joint structure. The load is attached to the end-effector using a thin wire as shown in Figure 15. When no weight is attached to the joint, the deflection of the joint (denoted in the figure by ‘D’) is taken as the zero-displacement reference. As the load increases, the value of deflection increases almost linearly until a bond break (yield point) occurs. The test is stopped at that point. Three trials are conducted for each joint and the average is plotted in Figure 16. Because the shaft does not mechanically move in the bonding state, the deflection that occurred before the yield point is caused by the elasticity of 3D printing material.

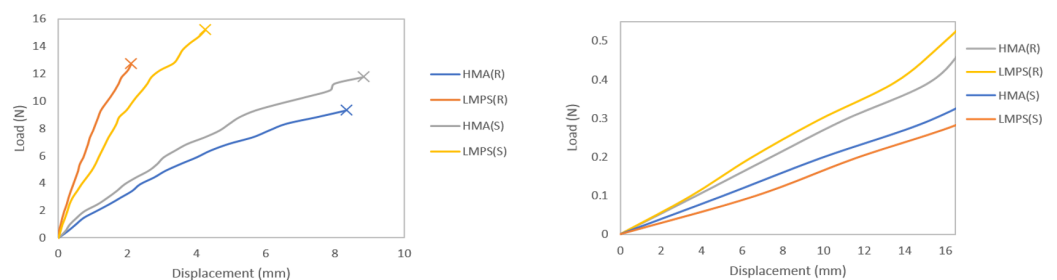


Figure 16. Load vs. displacement graph for the cantilevered TR-fluid-based joints in bonding state (left) and activated state (right). The yield points in bonding state are marked by ‘X’ on the left figure.

The average yield points of the revolute joints with HMA-based and LMPS-based bonding mechanisms are 9.47 N and 13.23 N, respectively. The average yield points for the spherical joints utilizing HMA-based and LMPS-based bonding mechanisms are 12.25 N and 16.01 N, respectively. The results indicate that the TR-fluid-based joints can support a payload equivalent to more than 25 times their weights (the average weight of a TR-fluid based joint is 38 g). The torque applied to the revolute and spherical joints at the yield point is calculated and listed in Table 4. The analytical results in Section 3 are compared to the experimental results, Figure 17. The results show that the model used in the analytical analysis provides good approximations of bonding torques. The same experiment with three trials for each joint is repeated in the activated state (TR-fluids are heated to their melting points). Figure 16 shows the average force required to deflect each of the four joints when TR fluids are activated. The joint deflection in this case depends fully on the design

structures, the deflection resistance is mainly due to the friction between shaft and base and the support from the bellows-like component.

Table 4. Bonding Torque Results at Yield Point.

Joint Type	LMPS Bonding Torque	HMA Bonding Torque
Revolute Joint	379.91 Nmm	262.32 Nmm
Spherical Joint	484.20 Nmm	370.56 Nmm

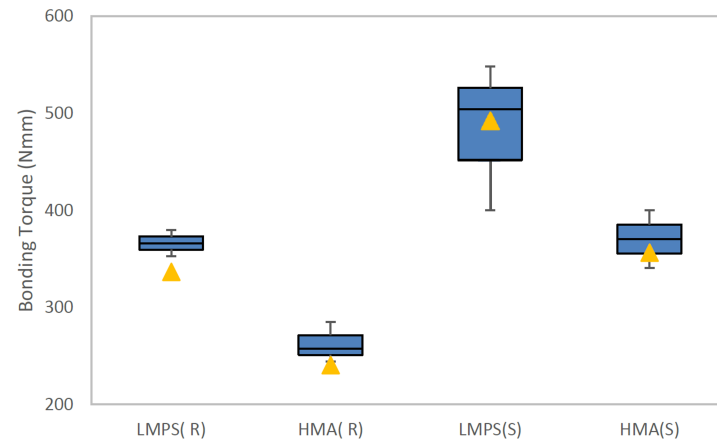


Figure 17. Box plot of the bonding torque of TR-fluid-based joints. Theoretical results (yellow triangles) and experimental results (blue squares).

The stiffness constant is calculated as the slope of the linear region in the load-displacement Figure 16. Computed stiffness constants of the four joint configurations in rigid and activated states are listed in Table 5. These values of stiffness constants are compared to the SolidWorks simulations in Section 3, Figure 18. In bonding state, the performed simulations provide a good prediction of the stiffness constant of LMPS-based revolute joint, while overestimating the value for other joints. The difference is a result of the assumptions made in the simulator. The base-shaft interface is assumed to be bonded, meaning that the TR-fluids do not contribute to the joint deflection. This is generally not true. For instance, we note during trials that the bonds formed by HMA pose some level of flexibility which can contribute to the deflection. In the activated state, the stiffness constants are computed similarly by computing the slopes in Figure 16(right) and compared to the simulation results in Figure 18. Joint simulations in the soft states provide overall good predictions of stiffness constants in all joint configurations. The stiffness increases for the bonding state compared to the soft state is quantified by computing the stiffness ratio. All joint configurations have a substantial increase in stiffness as shown in Table 5.

Table 5. Experimental Results of Stiffness Constant. ‘R’ and ‘S’ refer to revolute and spherical joints, respectively.

Joint Material	Stiffness Constant in Soft State (N/mm)	Stiffness Constant in Bonding State (N/mm)	Stiffness Increase Ratio
LMPS (R)	0.029 ± 0.0026	5.969 ± 1.5594	205.8
HMA (R)	0.026 ± 0.0013	1.228 ± 0.2332	47.2
LMPS (S)	0.017 ± 0.0004	3.669 ± 0.4678	215.8
HMA (S)	0.021 ± 0.0006	1.274 ± 0.1131	60.7

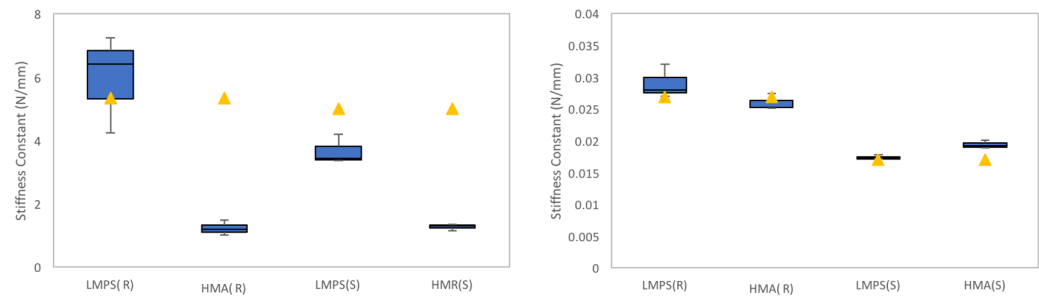


Figure 18. Box plot of the stiffness constant of TR-fluid-based joints in bonding state (left) and activated state (right). Theoretical results (yellow triangles) and experimental results (blue squares).

Table 6. Power Consumption, Activation Time, and Deactivation Time of the Four Joint Configurations.

	LMP(S)	HMA(R)	LMP(S)	HMA(S)
Power (W)	2.9 ± 0.2	3.7 ± 0.4	3.6 ± 0.1	2.7 ± 0.5
Activation Time (s)	13.0 ± 3.9	8.0 ± 1.5	29.4 ± 7.8	18.6 ± 2.5
Deactivation Time (s)	7.8 ± 1.9	42.7 ± 7.2	18.5 ± 2.8	30.2 ± 5.8

Response time is defined as the time for a single module to change between the rigid and soft states. The joint is cantilevered in a rigid state, and weight (500 g) is attached at the free end. Activation time is the time between turning on the resistive heating element and the moment the joint is fully flexible. The time and power consumption of 12 consecutive trials are shown in Table 6. HMA joints' activation times are smaller compared to LMP(S) joints since the bonding strength of HMA joints declines exponentially with temperature increase while the strength of LMP(S) bonds are slightly reduced with temperature prior to the yield point, matching the behaviour in our early testing, Figure 2. LMP(S)-based joints is faster to solidify compared to HMA-based joints. Note these times may not represent the state of the bond accurately, they are representing the state of the joint overall since there are no temperature sensors embedded inside the designed joints. Therefore, part of the deactivation time can be caused by overheating the joint before measuring deflection.

It is important to realise the TRF material and design limitations. Two possible failures are observed during the experimental trials. The detachment of the copper tapes from plastic components may occur before the break of the bond formed by LMP(S) or HMA. This can be mitigated by using high shear strength high-temperature resistance (above 80 °C) adhesive to attach the copper tapes. The shaft of the spherical joint occasionally breaks before the bond separation. This can be easily fixed by using materials with high yield strength to construct the shaft or increase its diameter. Furthermore, the revolute and spherical TRF joints response time in Table 6 makes them not suitable for applications where fast stiffness response is required. This can be mitigated by faster techniques to heat or better heat sink technologies or both.

6. Conclusions

This paper investigates the viability of using TR-fluids in the design of controllable stiffness joints. The designed joints employ thermally activated bonding mechanisms based on two TR fluids: LMP(S) and HMA. A testbed to characterize temperature response and repeatability of bonding materials is constructed. Experimental results of bonding torque and stiffness constant are compared to analytical modelling and simulation results. It is found that the developed model is a good representation of the actual joint and can predict bonding torques closely in all joint configurations. The developed joints have demonstrated a significant increase in stiffness in a deactivated state. The designed robotic joints have demonstrated a significant increase in stiffness at a rigid state supporting a

payload of more than 20 times their own weight which enables compact robot structures and opens opportunities for miniaturization. Future work will also focus on different techniques to embed heating devices and embedded temperature sensors which can help in detecting melting points, and therefore, enhance joint stiffness control and prevent overheating. Investigating faster heating and cooling technologies will be investigated to reduce response time and the effect of fast temperature change on materials will be studied. The developed TR-fluid joints will be used to construct a multi-joint snake robot where the dynamic bonding response of moving joints will be investigated.

Author Contributions: Conceptualization, A.A.D.-S. and R.C.R.; methodology, B.M. and R.C.R.; software, B.M. and M.Z.S.; validation, B.M.; formal analysis, M.Z.S.; investigation, B.M., R.C.R. and M.Z.S.; resources, A.A.D.-S. and R.C.R.; writing original draft, M.Z.S.; writing review and editing, M.Z.S. and R.C.R., visualisation, B.M. and M.Z.S.; supervision, A.A.D.-S. and R.C.R. All authors have read and agreed to the published version of the manuscript.

Funding: This research received no external funding.

Institutional Review Board Statement: Not applicable.

Informed Consent Statement: Not applicable.

Data Availability Statement: Numerical data and simulations are available for academic purposes upon request by contacting the authors.

Conflicts of Interest: All authors confirm that they have no conflict of interest, financial or otherwise.

References

- Ding, J.; Goldman, R.E.; Xu, K.; Allen, P.K.; Fowler, D.L.; Simaan, N. Design and coordination kinematics of an insertable robotic effectors platform for Single-Port access surgery. *IEEE/ASME Trans. Mechatron.* **2013**, *18*, 1612–1624. [[CrossRef](#)] [[PubMed](#)]
- Shang, J.; Payne, C.J.; Clark, J.; Noonan, D.P.; Kwok, K.W.; Darzi, A.; Yang, G.Z. Design of a multitasking robotic platform with flexible arms and articulated head for minimally invasive surgery. In Proceedings of the IEEE/RSJ International Conference on Intelligent Robots and Systems, Vilamoura-Algarve, Portugal, 7–12 October 2012; pp. 1988–1993.
- Kwok, K.W.; Tsoi, K.H.; Vitiello, V.; Clark, J.; Chow, G.; Luk, W.; Yang, G.Z. Dimensionality reduction in controlling articulated snake robot for endoscopy under dynamic active constraints. *IEEE Trans. Robot.* **2013**, *29*, 15–31. [[CrossRef](#)] [[PubMed](#)]
- Wright, C.; Buchan, A.; Brown, B.; Geist, J.; Schwerin, M.; Rollinson, D.; Tesch, M.; Choset, H. Design and architecture of the unified modular snake robot. In Proceedings of the IEEE International Conference on Robotics and Automation, Saint Paul, MN, USA, 14–18 May 2012; pp. 4347–4354.
- Wright, C.; Johnson, A.; Peck, A.; McCord, Z.; Naaktgeboren, A.; Gianfortoni, P.; Gonzales-Rivero, M.; Hatton, R.; Choset, H. Design of modular snake robot. In Proceedings of the IEEE International Conference on Intelligent Robots and Systems, San Diego, CA, USA, 29 October–2 November 2007; pp. 2609–2614.
- Mehling, J.S.; Diftler, M.A.; Chu, M.; Valvo, M. A minimally invasive tendril robot for in-space inspection. In Proceedings of the IEEE/RAS-EMBS International Conference on Biomedical Robotics and Biomechanics, Pisa, Italy, 20–22 February 2006; pp. 690–695.
- Gravagne, I.A.; Walker, I.D. Large deflection dynamics and control for planar continuum robots. *IEEE/ASME Trans. Mechatron.* **2003**, *8*, 299–307. [[CrossRef](#)]
- Mahvash, M.; Zenat, M. Toward a hybrid snake robot for single-port surgery. In Proceedings of the Annual International Conference of the IEEE Engineering in Medicine and Biology Society, Boston, MA, USA, 30 August–3 September 2011; pp. 5372–5375.
- Trivedi, D.; Rahn, C.D.; Kier, W.M.; Walker, I.D. Soft robotics: Biological inspiration, state of the art, and future research. *Appl. Bionics Biomech.* **2008**, *5*, 99–117. [[CrossRef](#)]
- Kim, S.; Laschi, C.; Trimmer, B. Soft robotics: A bioinspired evolution in robotics. *Trends Biotechnol.* **2013**, *31*, 287–294. [[CrossRef](#)]
- Simaan, N.; Taylor, R.; Flint, P. High Dexterity Snake-like Robotic Slaves for Minimally Invasive Telesurgery of the Upper Airway. In Proceedings of the International Conference on Medical Image Computing and Computer-Assisted Intervention, St. Malo, France, 26–29 September 2004; pp. 17–24.
- Simaan, N.; Taylor, R.; Flint, P. A dexterous system for laryngeal surgery. In Proceedings of the IEEE International Conference on Robotics and Automation, New Orleans, LA, USA, 26 April–1 May 2004; pp. 351–357.
- Degani, A.; Choset, H.; Wolf, A.; Zenat, M.A. Highly Articulated Robotic Probe for Minimally Invasive Surgery. In Proceedings of the IEEE International Conference on Robotics and Automation, Orlando, FL, USA, 15–19 May 2006; pp. 4167–4172.
- Degani, A.; Choset, H.; Wolf, A.; Ota, T.; Zenati, M.A. Percutaneous Intrapericardial Interventions Using a Highly Articulated Robotic Probe. In Proceedings of the IEEE / RAS-EMBS International Conference on Biomedical Robotics and Biomechanics, Pisa, Italy, 20–22 February 2006; pp. 7–12.

15. Chen, Y.; Chang, J.H.; Greenlee, A.S.; Cheung, K.C.; Slocum, A.H.; Gupta, R. Multi-turn, tension-stiffening catheter navigation system. In Proceedings of the IEEE International Conference on Robotics and Automation, Anchorage, AK, USA, 3–7 May 2010; pp. 5570–5575.
16. Manti, M.; Cacucciolo, V.; Cianchetti, M. Stiffening in soft robotics: A review of the state of the art. *IEEE Robot. Autom.* **2016**, *23*, 93–106. [[CrossRef](#)]
17. Majidi, C.; Wood, R.J. Tunable elastic stiffness with micro-confined magnetorheological domains at low magnetic field. *Appl. Phys. Lett.* **2010**, *97*, 164104. [[CrossRef](#)]
18. Liu, B.; Boggs, S.A.; Shaw, M.T. Electrorheological Properties of Anisotropically Filled Elastomers. *IEEE Trans. DEI* **2001**, *8*, 173–181. [[CrossRef](#)]
19. Cao, C.; Zhao, X. Tunable stiffness of electrorheological elastomers by designing mesostructures. *Appl. Phys. Lett.* **2013**, *103*, 041901. [[CrossRef](#)]
20. Cheng, N.; Ishigami, G.; Hawthorne, S.; Hao, C.; Hansen, M.; Telleria, M.; Playter, R.; Iagnemma, K. Design and analysis of a soft mobile robot composed of multiple thermally activated joints driven by a single actuator. In Proceedings of the IEEE International Conference on Robotics and Automation, Anchorage, AK, USA, 3–7 May 2010; pp. 5207–5212.
21. Telleria, M.; Hansen, M.; Campbell, D.; Servi, A.; Culpepper, M. Modeling and implementation of solder-activated joints for single-actuator, centimeter-scale robotic mechanisms. In Proceedings of the IEEE International Conference on Robotics and Automation, Anchorage, AK, USA, 3–7 May 2010, pp. 1681–1686.
22. Neubert, J.; Rost, A.; Lipson, H. Self-soldering connectors for modular robots. *IEEE Trans. Robot.* **2014**, *30*, 1344–1357. [[CrossRef](#)]
23. Cheng, N.G.; Gopinath, A.; Wang, L.; Iagnemma, K.; Hosoi, A.E. Thermally tunable, self-healing composites for soft robotic applications. *Macromol. Mater. Eng.* **2014**, *299*, 1279–1284. [[CrossRef](#)]
24. Cheng, N.G.; Lobovsky, M.B.; Keating, S.J.; Setapen, A.M.; Gero, K.I.; Hosoi, A.E.; Iagnemma, K.D. Design and analysis of a robust, low-cost, highly articulated manipulator enabled by jamming of granular media. In Proceedings of the IEEE International Conference on Robotics and Automation, St. Paul, MN, USA, 14–18 May 2012; pp. 4328–4333.
25. Cianchetti, M.; Ranzani, T.; Gerboni, G.; Falco, I.D.; Laschi, C.; Menciassi, A. STIFF-FLOP Surgical Manipulator: Mechanical design and experimental characterization of the single module. In Proceedings of the IEEE/RSJ International Conference on Intelligent Robots and Systems, Tokyo, Japan, 3–7 November 2013; pp. 3576–3581.
26. Ranzani, T.; Cianchetti, M.; Gerboni, G.; Falco, I.D.; Menciassi, A. A Soft Modular Manipulator for Minimally Invasive Surgery: Design and Characterization of a Single Module. *IEEE Trans. Robot.* **2016**, *32*, 187–200. [[CrossRef](#)]
27. Kim, Y.J.; Cheng, S.; Kim, S.; Iagnemma, K. Design of a tubular snake-like manipulator with stiffening capability by layer jamming. In Proceedings of the International Conference on Intelligent Robots and Systems, Vilamoura-Algarve, Portugal, 7–12 October 2012; pp. 4251–4256.
28. Kim, Y.J.; Cheng, S.; Kim, S.; Iagnemma, K. A novel layer jamming mechanism with tunable stiffness capability for minimally invasive surgery. *IEEE Trans. Robot.* **2013**, *29*, 1031–1042. [[CrossRef](#)]
29. Wang, L.; Iida, F. Physical connection and disconnection control based on hot melt adhesives. *IEEE/ASME Trans. Mechatron.* **2013**, *18*, 1397–1409. [[CrossRef](#)]
30. Wang, L.; Graber, L.; Iida, F. Large-payload climbing in complex vertical environments using thermoplastic adhesive bonds. *IEEE Trans. Robot.* **2013**, *29*, 863–874. [[CrossRef](#)]
31. Shintake, J.; Schubert, B.; Rosset, S.; Shea, H.; Floreano, D. Variable stiffness actuator for soft robotics using dielectric elastomer and low-melting-point alloy. In Proceedings of the IEEE/RSJ International Conference on Intelligent Robots and Systems, Hamburg, Germany, 28 September–2 October 2015; pp. 1097–1102.
32. Schubert, B.E.; Floreano, D. Variable stiffness material based on rigid low-melting-point-alloy microstructures embedded in soft polydimethylsiloxane (PDMS). *RSC Adv.* **2013**, *3*, 24671–24679. [[CrossRef](#)]
33. Lin, Y.; Yang, G.; Liang, Y.; Zhang, C.; Wang, W.; Qian, D.; Yang, H.; Zou, J. Controllable stiffness origami “skeletons” for lightweight and multifunctional artificial muscles. *Adv. Funct. Mater.* **2020**, *30*, 2000349. [[CrossRef](#)]
34. Yang, Y.; Chen, Y. Novel design and 3D printing of variable stiffness robotic fingers based on shape memory polymer. In Proceedings of the 2016 6th IEEE International Conference on Biomedical Robotics and Biomechatronics (BioRob), Singapore, 26–29 June 2016.
35. Li, X.; Zhu, H.; Lin, W.; Chen, W.; Low, K. Structure-Controlled Variable Stiffness Robotic Joint Based on Multiple Rotary Flexure Hinges. *IEEE Trans. Ind. Electron.* **2020**, *68*, 12452–12461. [[CrossRef](#)]
36. SMOOTH-ON. Technical and Buying Information. Available online: <https://www.smooth-on.com/product-line/dragon-skin/> (accessed on 28 April 2022).
37. Huat, L.J. Customizable Soft Pneumatic Gripper Devices. Master’s Thesis, National University of Singapore, Singapore, 2015.
38. Sparks, J.L.; Vavalle, N.A.; Kasting, K.E.; Long, B.; Tanaka, M.L.; Sanger, P.A.; Schnell, K.; Conner-Kerr, T.A. Use of silicone materials to simulate tissue biomechanics as related to deep tissue injury. *Adv. Skin Wound Care* **2015**, *28*, 59–68. [[CrossRef](#)]
39. Martins, P.A.L.S.; Jorge, R.M.N.; Ferreora, A.J.M. A comparative study of several material models for prediction of hyperelastic properties: 73 application to silicone-rubber and soft tissues. *Strain* **2006**, *42*, 135–147. [[CrossRef](#)]
40. Meghezi, S.; Couet, F.; Chevallier, P.; Mantovani, D. Effects of a pseudophysiological environment on the elastic and viscoelastic properties of collagen gels. *Int. J. Biomater.* **2012**, *2012*, 319290. [[CrossRef](#)] [[PubMed](#)]

41. Ali, A.; Hosseini, M.; Sahari, B.B. A review of constitutive models for rubber-like materials. *Am. J. Eng. Appl. Sci.* **2010**, *3*, 232–239. [[CrossRef](#)]
42. Case, J.; White, E.; Kramer, R. Soft material characterization for robotic applications. *Soft Robot.* **2015**, *2*, 80–87. [[CrossRef](#)]
43. Marechal, L.; Baland, P.; Lindenroth, L.; Petrou, F.; Kontovounisios, C.; Bello, F. Toward a common framework and database of materials for soft robotics. *Soft Robot.* **2021**, *8*, 284–297. [[CrossRef](#)] [[PubMed](#)]
44. *ASTM Standard D412, 06a*. Standard Test Methods for Vulcanized Rubber and Thermoplastic Elastomers-Tension; ASTM International: West Conshohocken, PA, USA, 2013.